Results in Physics 76 (2025) 108415

Contents lists available at ScienceDirect

Results in Physics

journal homepage: www.elsevier.com/locate/rinp

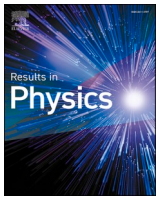

Comparative study of ablation processes using femtosecond and nanosecond lasers

J.Z. Wang [a,*], Y. Kanematsu [a,b], A. Muratsugu [c], F. Matsuda [d], W. Matsuda [b], Y. Kawai [b], M. Toyoda [a,b]

[a] Department of Physics, Graduate School of Science, The University of Osaka, 1-1 Machikaneyama, Toyonaka, Osaka 560-0043, Japan
[b] Forefront Research Center, Graduate School of Science, The University of Osaka, 1-1 Machikaneyama, Toyonaka, Osaka 560-0043, Japan
[c] Atelier Monotrem, Suita, Osaka 564-0001, Japan
[d] Institute for Integrated Cell-Material Sciences (iCeMS), Kyoto University, Yoshida-honmachi, Sakyo-ku, Kyoto 606-8501, Japan

A B S T R A C T

This study investigated the dynamic characteristics of ions emitted from materials subjected to short-pulsed laser interactions. To investigate the difference in ablation dynamics due to laser pulse irradiation with the same energy but different time scales, we developed a time-of-flight (TOF) mass spectrometer and analyzed the TOF ion profiles obtained by irradiating 180 fs 800 nm Ti:sapphire femtosecond laser and 1 ns 355 nm Nd:YAG nanosecond laser. The effects of incident laser interaction with CsI deposits were examined for laser pulse energies ranging from 400 to 1000 nJ, corresponding to laser intensities of 7.1×10^{11}–1.8×10^{12} W/cm^2 for femtosecond lasers and 1.3–3.2 $\times 10^8$ W/cm^2 for nanosecond lasers. With an ion trajectory simulation incorporating a shifted Maxwell–Boltzmann initial velocity distribution and continuous ion emission, we analyzed the ion emission dynamics from the TOF profiles. Compared with nanosecond lasers, femtosecond lasers generated ions with higher initial velocities but lower temperatures. Under nanosecond laser irradiation, ion emission continued for tens of nanoseconds after the end of the laser pulse, and its duration increased with increasing laser pulse energy. However, no continuous emission occurred under femtosecond laser irradiation.

Introduction

Over the past 20 years, femtosecond laser-produced plasma (LPP) has been studied for a wide range of industrial and academic applications [1–3] such as pulsed laser deposition [4], laser-induced breakdown spectroscopy [5], laser ablation inductively coupled plasma mass spectrometry [6], and ion implantation [7]. The pulse interaction mechanism of femtosecond (fs) laser with a solid target is fundamentally different to that of nanosecond (ns) laser because of its ultrashort irradiation periods and ultrahigh intensities [8,9]. For ns laser, material transformation with a long period and low intensity (10^8–10^9 W/cm^2) pulse proceeds in thermal equilibrium between electrons and ions [10]. A large part of laser energy is deposited into the plasma plume generated by a continuous energy transfer from electrons to ions of the target material through electron–phonon collisions, resulting in continuum plasma expansion that lasts up to hundreds of nanoseconds [11]. For fs laser, the intensity is typically between 10^{10} and 10^{16} W/cm^2. When the laser intensity exceeds the ablation threshold of the target material (around 10^{13}–10^{14} W/cm^2), the initial nonequilibrium process of laser–matter interaction occurring within the first 100 fs involves electrostatic ablation. Specifically, the target surface electrons absorb the pulse energy and escape, generating a strong electrostatic field that extracts and accelerates a small number of ions from the target. During this process, the extracted ions remain cold, inhibiting conventional thermal expansion [12,13]. After 100 fs, the interaction proceeds to a transitional state, where electron–phonon and electron–ion collisions occur in picoseconds, causing a large number of ions to be emitted [14,15].

To compare and characterize ion emission processes induced by fs and ns laser ablation, optical emission spectroscopy has been widely employed in previous studies, often accompanied by intensified charge-coupled device fast photography [16,17]. These techniques allow to measure LPP parameters, such as excitation temperatures, electron density, species distributions, and time and spatial distributions. In addition, various studies have employed time-of-flight (TOF) profiles to investigate ion emission using Langmuir probes [18], Faraday cups [19], electrostatic energy analyzers [20,21], and TOF mass spectrometers [22]. In these methods, the velocity distribution of ions emitted by a single laser shot can be captured from the ion flight distance and TOF measurements. Most studies using TOF profiles assume that the ion production time scale is negligible compared with the time to accelerate and TOF of ions [23]. However, optical emission spectroscopy has

* Corresponding author.
E-mail address: wjz@mass.phys.sci.osaka-u.ac.jp (J.Z. Wang).

https://doi.org/10.1016/j.rinp.2025.108415
Received 4 June 2025; Received in revised form 28 July 2025; Accepted 26 August 2025
Available online 27 August 2025

demonstrated that the lifetime of the LPP extends beyond the duration of the laser pulse [24,25]. Nevertheless, TOF-based investigations have generally not fully considered the potential effects of the LPP lifetime on the initial velocity distributions of emitted ions. Such an oversight may result in an incomplete characterization of ion emission dynamics.

In this study, we developed a TOF mass spectrometer to study ion emission under ns (10^8 W/cm^2) and fs (10^{10}–10^{12} W/cm^2) laser irradiation, focusing on the differences in ablation dynamics arising from the application of the same pulse energy over different time scales. To better understand ion emission, we conducted ion trajectory simulation with the initial ion velocity distribution represented by a shifted Maxwell–Boltzmann distribution (SMBD) [26] and Gaussian distribution representing continuous ion emission.

Experimental methods

Experimental setup

The schematic of the developed experimental setup is shown in Fig. 1. The setup comprises a laser system and TOF mass spectrometer. A Ti:sapphire fs laser system (Rega 9000, Coherent, USA) delivers 180 fs pulses at a 10–200 kHz repetition rate and center wavelength of 800 nm. The Rega 9000 amplifier is seeded with the mode-locked oscillator and pumped by a Nd:YVO_4 laser. The pump laser also pumps the oscillator. The laser pulses are introduced into a prism pair for group velocity dispersion compensation to control the laser pulse duration. The femtosecond pulse (800 nm) train is divided into two parts by a beam splitter. To ensure precise timing synchronization in ion TOF measurements, one pulse train is focused on the β-BaB_2O_4 crystal to generate a 400 nm second harmonic, which is detected by a silicon photodiode to produce a reliable trigger signal for an oscilloscope. The other pulse train is focused onto the sample plate of the TOF mass spectrometer with a spot diameter of 20 μm. A passively Q-switched Nd:YAG ns laser system (FTSS 355–50, CryLas, Germany) outputs a wavelength of 355 nm and 1 ns laser pulses at a repetition rate of 200 Hz. The nanosecond pulse (355 nm) train is similarly divided into two parts by a beam splitter. One ns pulse train is detected by the silicon photodiode to produce a trigger signal for the oscilloscope synchronization, while the other pulse train is focused onto the sample plate with a spot diameter of 20 μm. Both fs and ns laser irradiations are performed under high-vacuum conditions (~10^{-5} Pa). The laser irradiation position on the sample plate is controlled by Galvano mirrors. The pulse energy of the fs laser is directly measured at the sample surface using a power meter (OPM-572, SANWA, JAPAN) before the measurement, ensuring that the reported pulse energy corresponds to the actual fluence at the ablation site. Similarly, the ns laser energy is measured at the sample surface with a power meter (PM-245, NEOARK, JAPAN). The pulse energies of both fs and ns lasers are adjusted using an optical filter. Note that although different wavelengths are used for fs and ns lasers, the wide band gap energy (5.4–5.9 eV [27]) of the CsI sample allows the photothermal mechanism to dominate for both UV and IR laser irradiation; therefore, the difference in wavelength is not a significant factor in comparing the ablation process with ns and fs laser irradiation. Details are given in Sec. 3.

A voltage of 3.0 kV is applied to the sample plate, and the emitted ions are accelerated between the sample plate and grounded aperture-shaped acceleration electrode. Through a 193 mm free drift region, the ions are separated on their mass-to-charge ratio and detected by a microchannel plate detector (F12334-11, Hamamatsu Photonics, Japan). Since a positive extraction voltage is applied to the sample plate, only positively charged ions are accelerated and detected. The detected ion signals are acquired by a 1 GHz digital oscilloscope (DSO7104A, Agilent, USA) and transferred to a computer as waveform data. After the computer receives the waveform data from the oscilloscope, we obtain TOF spectra through a signal-averaging method. Each TOF spectrum is obtained by accumulating waveforms for a specific number of laser shots to reduce random noise.

Sample preparation

We select cesium iodide (CsI) as the sample. CsI has a simple chemical composition with both atomic species being monoisotopic, which simplifies mass spectrometric analyses and is convenient for the study of the physical aspects of the ablation process [28]. CsI is deposited at a thickness of 1000 nm under a pressure of 2.0×10^{-5} Pa with a deposit velocity of 0.2–0.4 nm/s using a physical vapor deposition equipment (Knenix, KVD-670, Japan). From atomic force microscopy, the surface roughness is evaluated to be within 1 μm, which corresponds

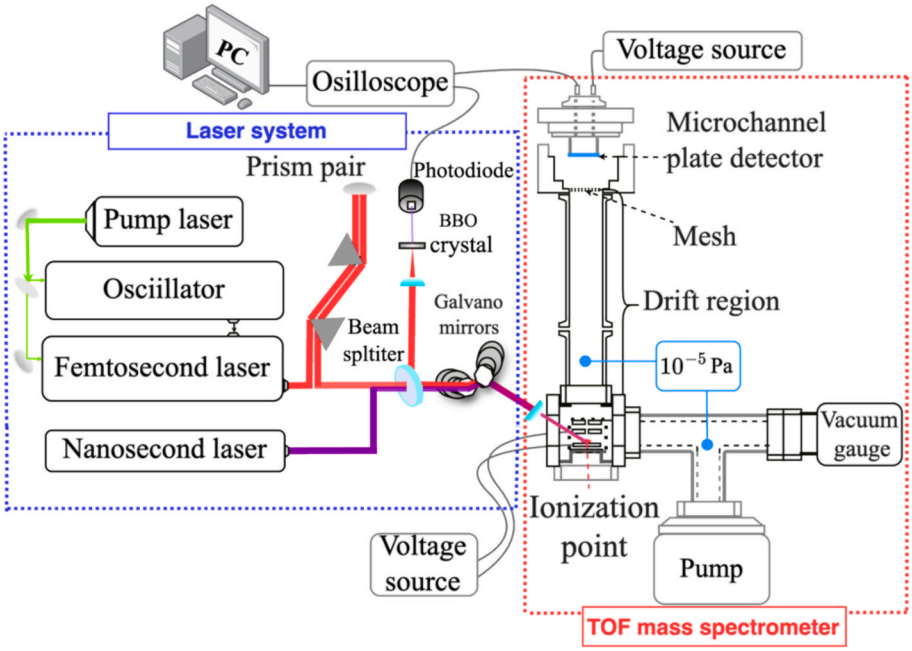

Fig. 1. Schematic of experimental setup involving TOF mass spectrometer and laser system.

to a TOF difference of less than 1 ns.

Ion trajectory simulation

To observe the ion temperature and initial velocity under different laser pulse energies and durations, we conduct an ion trajectory simulation based on the ion source structure and dimensions. As shown in Fig. 2, the ion source consists of a sample plate and two coaxially aligned aperture-shaped plates. The sample is mounted on a 1.5 mm-thick 34 mm-diameter aluminum plate biased at 3.0 kV. The first aperture plate is positioned 11.0 mm away from the sample plate and biased at 0.0 kV. The second aperture plate is located 5.5 mm away and held at ground potential. Both aperture plates are 2.0 mm in thickness and 34.0 mm in diameter, with central aperture diameters of 2.4 and 2.9 mm, respectively. Ions are extracted through these apertures and accelerated into the drift region.

The electrostatic potential distribution of the ionization source of the TOF mass spectrometer is obtained with the surface charge method [29], and the ion trajectory is calculated using the fourth-order Runge–Kutta method. We assume that the initial velocity distribution of the emitted ions follows a two-dimensional shifted Maxwell–Boltzmann distribution (SMBD) defined as

$$f(v_z) = \left(\frac{m_i}{2\pi k_B T_i}\right)^{\frac{1}{2}} \exp\left[-\frac{m_i}{2k_B T_i}\left(v_z - v_{shifted}\right)^2\right], \quad (1)$$

$$f(v_r) = \left(\frac{m_i}{2\pi k_B T_i}\right)^{\frac{1}{2}} \exp\left[-\frac{m_i}{2k_B T_i} v_r^2\right]. \quad (2)$$

Eq. (1) was proposed by Torrisi et al. [26]. Here, $v_{shifted}$ is the center-of-mass velocity of the expanding plasma that is a combination of plasma adiabatic expansion velocity and Coulomb acceleration velocity [30]. In addition, T_i is the ion temperature, m_i is the ion mass, k_B is the Boltzmann constant, v_z is the velocity component perpendicular to the sample surface, and v_r is the radial (in-plane) velocity component.

In addition to the SMBD, we introduce a model in which ions are continuously emitted from the sample surface over a finite period following a laser pulse, allowing to accurately reproduce the experimental results. This model accounts for two scenarios. In one scenario, all N ions are emitted at the end of the laser pulse $t_0 = 0$, while in the other scenario, N ions are continuously emitted beyond t_0 following a Gaussian distribution. In this model, the emission rate of ions, $n(t)$, is expressed as

$$n\left(t\right) = \begin{cases} N, & t_0 = 0, \\ \dfrac{N}{\sqrt{2\pi\sigma^2}} \exp\left[-\dfrac{(t-\mu)^2}{2\sigma^2}\right], & 0 \le t \le t_0 \text{ and } t_0 > 0, \end{cases} \quad (3)$$

where μ and σ are determined to be $t_0/2$ and $t_0/6$, respectively. This ensures that range $[\mu - 3\,\sigma, \mu + 3\,\sigma]$ corresponds to $[0, t_0]$, accounting for all emitted ions within period t_0.

For fitting to each experimentally obtained TOF spectrum, we conduct ion trajectory simulations by changing $v_{shifted}$, T_i, and t_0. These parameters are varied such that the full width at half maximum (FWHM) and peak positions of the calculated TOF spectra are equal to the experimental results. The explored parameter space is T_i = 1000–100,000 K (increment of 1000 K), $v_{shifted}$ = 500–20,000 m/s (increment of 100 m/s), and t_0 = 0–100 ns (increment of 1 ns). These parameter ranges are chosen from previous experimental and theoretical studies [26,31]. For each parameter set (T_i, $v_{shifted}$, t_0), we simulate N = 40,000 ions. The emission rate of ions is assigned according to the temporal profile in Eq. (3) characterized by t_0, while initial velocities are sampled from Eqs. (1) and (2) determined by T_i and $v_{shifted}$. The resulting TOF spectra are statistically analyzed and normalized. A successful fit is defined by two criteria. 1) The FWHM of the simulated TOF spectrum matches the experimental FWHM within a tolerance of < 1 ns. 2) The peak position of the simulated TOF spectrum aligns with the experimental peak within < 1 ns. The 1 ns tolerance is selected based on the temporal resolution of the oscilloscope. To estimate the uncertainty associated with each fitting parameter, T_i, $v_{shifted}$, and t_0 are independently varied to determine the minimum change that produces a deviation of 1 ns in either the FWHM or peak position of the simulated TOF spectrum. The resulting uncertainties are $v_{shifted} = \pm$ 100 m/s and $t_0 = \pm$ 1 ns, while the uncertainty in T_i is $\pm$ 500 K for $t_0 = 0$ and $\pm$ 5000 K for $t_0 > 0$.

Experimental results and discussion

We introduced 400 shots of fs/ns laser pulses to deposited CsI and accumulated the ion signals to obtain the TOF spectrum of Cs^+. To investigate the laser intensity dependence on the emitted ion parameters, the measurements were conducted with pulse energies of 400, 500, 800, and 1000 nJ, corresponding to a laser intensity range of 7.1 $\times$ 10^{11}–1.8 $\times$ 10^{12} W/cm^2 for fs lasers and 1.3–3.2 $\times$ 10^8 W/cm^2 for ns lasers. After obtaining the TOF spectrum of Cs ions with different laser intensities, we fitted them to the corresponding SMBD with continuous ion emission using the abovementioned procedure and determined ion temperature T_i, shifted center-of-mass velocity $v_{shifted}$, and ion emission duration t_0. Without considering continuous ion emission, the SMBD alone could not reproduce the experimental results for the ns laser. In fact, initial velocity v_0 was less than 0 m/s as calculated from the TOF using the following equation based on a one-dimensional approximation:

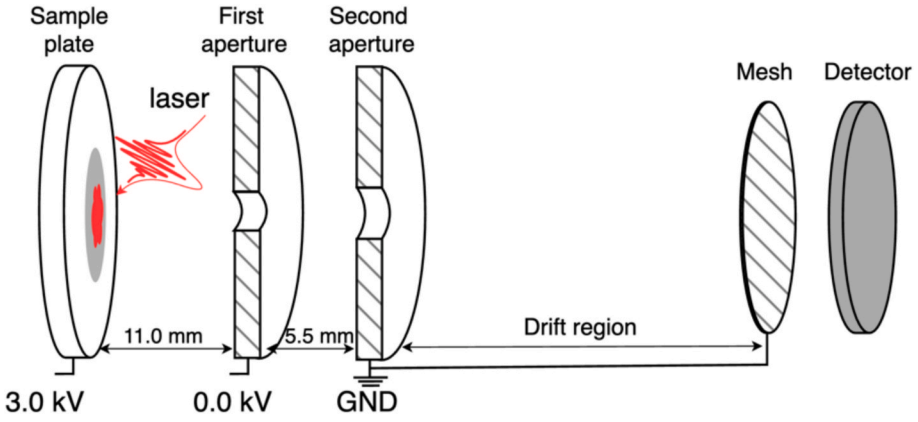

Fig. 2. Schematic of ion source and acceleration region in TOF mass spectrometer. The sample is mounted on a 2.0 mm-thick 34.0 mm-diameter aluminum plate (3.0 kV). Ions are extracted through two coaxially aligned aperture plates (0.0 kV and grounded) and accelerated into the drift region.

$$TOF = \frac{-v_0 + \sqrt{v_0^2 + 2Uq/m}}{Uq/mL_1} + \frac{L_2}{\sqrt{v_0^2 + 2Uq/m}}, \quad (4)$$

where the ion with initial velocity v_0 and mass-to-charge ratio (m/q) traverses through an acceleration region L_1 with acceleration voltage U and field-free region L_2. This suggests the validity of our model in which ions are sequentially emitted from the sample surface over a finite period following the laser pulse.

The number of Cs^+ ions emitted by each laser pulse was estimated based on the detected Cs^+ signal intensity. The signal peak area due to the detection of a single Cs^+ ion is 3.4 mV·ns on average. By dividing the peak area of the TOF spectrum of Cs^+ by 3.4 mV·ns, the number of detected Cs^+ ions per laser pulse was calculated.

The obtained TOF profiles for fs and ns laser irradiation are shown in Fig. 3. The experimental results are represented by solid lines, and the results of the fitted ion trajectory simulations are shown as bar graphs. The obtained parameters, T_i, $v_{shifted}$, t_0, and ion count per laser pulse (average over 400 pulses) are summarized in Table 1. The error ranges of the parameters are described above.

The obtained $v_{shifted}$ for the fs laser irradiation was always higher than that for ns laser irradiation. Similar ion kinetic energies ($v_{shifted}$ = 4300–5200 m/s corresponding to 12.7–18.6 eV) have been reported in other fs laser ablation studies performed under comparable or even higher intensity conditions. For instance, Mannion et al. [32] observed ion kinetic energy distributions of 0–20 eV for Ag, Ni, and Al using 200 fs laser pulses at an intensity of 3.3×10^{12} W/cm^2, and Kelly et al. [19] reported 20 eV carbon ion emission under 70 fs laser pulses at 5.6×10^{12} W/cm^2. These findings support the plausibility of our observed kinetic energy.

We estimated the kinetic energy of Cs^+ generated using fs laser. When fs laser penetrates a solid surface, the laser electric field penetrates a characteristic depth of skin layer l_s due to the skin effect [33]. Within l_s, laser electric field intensity $E(z)$ decays exponentially as it propagates deeper into the solid as $E(z) = E(0)\exp[-z/l_s]$. Electrons absorb the laser energy through inverse bremsstrahlung and resonance absorption [15], thereby increasing the electron temperature. Through the energy conservation law, electron temperature $T_e(z,t)$ in the skin layer can be expressed as [15]

$$T_e(z,t) = \frac{16\pi I_0 t}{3\lambda n_e} \exp\left[-\frac{2z}{l_s}\right], \quad (5)$$

where n_e is the electron density, λ is the laser wavelength, and I_0 is the laser intensity. Once the energy of the electrons reaches the sum of binding energy ε_b and ionization potential J_i, they escape the solid surface. This process generates a charge separation between the escaped electrons and remaining ions, leading to the formation of a strong electric field. The ions are ejected from the target and accelerated in the electric field. The maximum energy of ions, ε_i, extracted from the surface reaches [15]

$$\varepsilon_i \approx T_e - J_i - \varepsilon_b. \quad (6)$$

Assuming that each ionized CsI molecule in the crystal releases one free electron upon laser irradiation, we estimated $n_e = 1 \times 10^{22}$ cm^{-3}. This assumption was based on the complete ionization of CsI under the given laser conditions, where Cs^+ and I^- were fully dissociated, and the valence electrons were released into the vacuum. By incorporating known parameters J_i = 7.1 eV [34], ε_b = 3.3 eV [35], single pulse duration t = 180 fs, and intensity $I_0 = 7.1 \times 10^{11}$ W/cm^2 (400 nJ) into Eqs. (5) and (6) and considering depth z to approach 0, the Cs^+ ion emission kinetic energy from the target surface layer was determined to be ε_i = 4.7 eV. This value was approximately one-quarter of the experimentally measured kinetic energy of 18.6 eV. This discrepancy suggests the contribution of additional energy from other nonthermal processes,

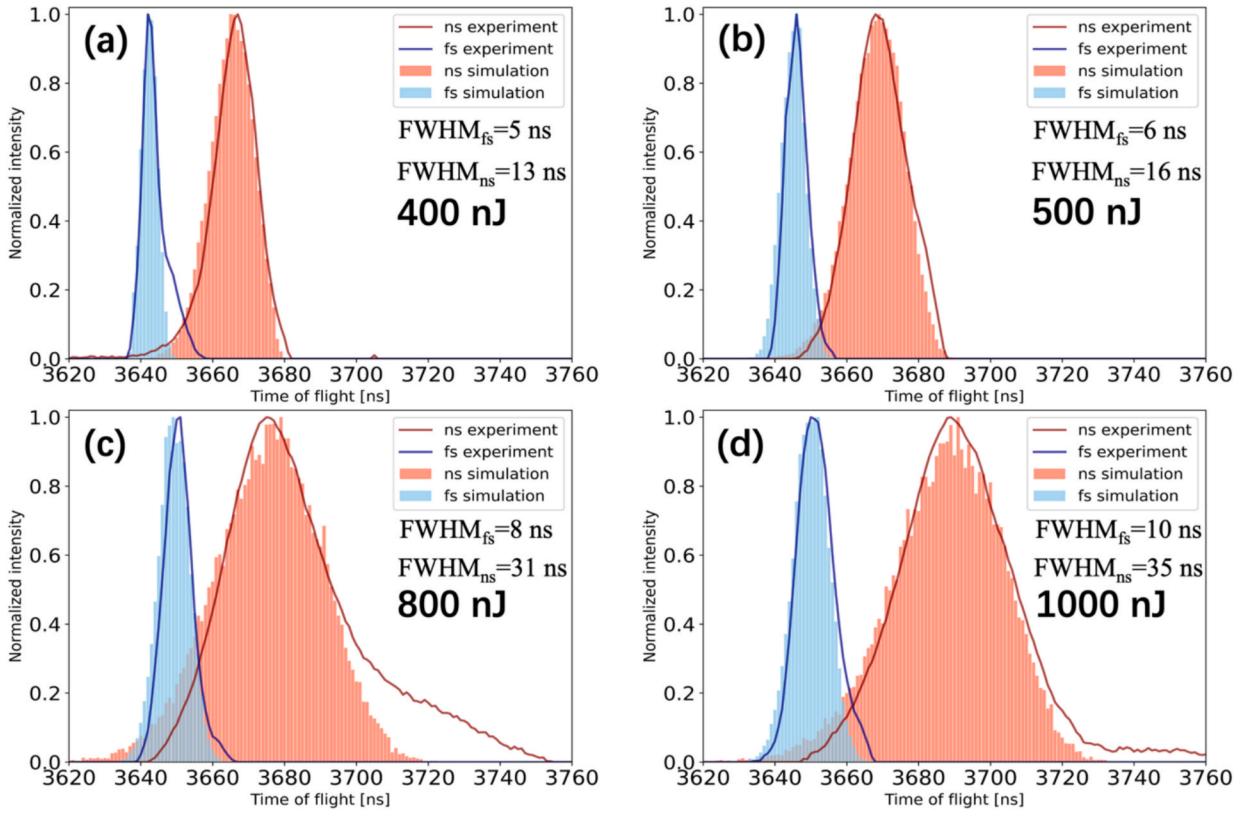

Fig. 3. TOF spectra of Cs^+ ions under different laser pulse energies. Panels (a)–(d) correspond to laser pulse energies of 400, 500, 800, and 1000 nJ, respectively. In each panel, the solid lines represent the experimental results and the bars represent the simulation results. Red and blue indicate the results under ns and fs laser irradiation, respectively. The FWHM values of the TOF spectra ($FWHM_{ns}$ and $FWHM_{fs}$) and corresponding laser pulse energy are indicated in each panel.

Table 1
Fitting parameters obtained from fitting SMBD of velocity and Gaussian temporary ion emission distribution to Cs^+ TOF profiles and ion count per laser pulse (average over 400 pulses).

Laser Energy (nJ)	fs laser T_i(× 10^3 K)	$v_{shifted}$(m/s)	t_0(ns)	Ion count/pulse	T_i(× 10^3 K)	ns laser $v_{shifted}$(m/s)	t_0(ns)	Ion count/pulse
400	1.0	5200	0	15	14	2200	0	172
500	2.5	4800	0	13	18	2800	11	500
800	4.5	4300	0	66	38	4300	51	9583
1000	6.0	4300	0	161	60	2600	57	7753

such as Coulomb explosion [36].

In the laser fluence range in this experiment, fs pulse ablation is typically governed by "cold ablation" mechanisms, such as desorption and photomechanical spallation [37,38]. The laser fluence range of 128–160 mJ/cm^2 (corresponding to laser pulse energies of 400–500 nJ) is below the ablation threshold of ~ 250 mJ/cm^2 for CsI [39], suggesting that desorption is the main ion emission mechanism. The fluence range of 256–320 mJ/cm^2 (corresponding to 800–1000 nJ) slightly exceeds the ablation threshold, and a pulse duration of 180 fs satisfies the stress confinement condition ($\tau_p \leq \tau_s \sim l_s/C_s$), where τ_p is the pulse duration, C_s is the speed of sound in the irradiated material, and τ_s is the characteristic time for mechanical equilibration of the absorbing volume. Thus, photomechanical spallation is a plausible ablation mechanism. A phase explosion occurs when the fluences are significantly higher than 1 J/cm^2 [40], but such a high fluence was not reached in this experiment.

In contrast to fs laser, the ns laser results exhibited drastically different trends. As listed in Table 1, for a laser energy of 400 nJ, ion temperature T_i for ns laser (1.4 × 10^4 K) was an order of magnitude higher than that for fs laser (1.0 × 10^3 K). In addition, the ns laser produced higher ion counts per laser pulse irradiation than the fs laser under the same pulse energy. This difference highlights the much greater efficiency of the ns laser in producing ions under thermal ablation conditions. This difference arises from the distinct energy transfer mechanisms governing the two ablation regimes. The long pulse duration in the order of nanoseconds allows sufficient time for energy transfer from the electrons to the lattice via electron–phonon coupling in the order of picoseconds. This enables uniform heating and phase transitions (melting and vaporization) of the target material, resulting in higher ion temperatures and enhanced ion emissions. However, the ultrashort pulse in the order of femtoseconds deposits energy into electrons faster than the electron–phonon relaxation time, thus preventing energy transfer to the lattice. Instead, material removal is dominated by nonthermal mechanisms of electrostatic ablation, where ions are accelerated in the electric field caused by charge separation created by energetic electrons escaping from the target without large lattice heating, as described above. This nonthermal process results in a lower ion temperature and fewer ion counts per laser pulse under the same pulse energy conditions compared to ns lasers.

Furthermore, the FWHM of the TOF profiles behaves differently for ns and fs lasers. For fs laser, the FWHM broadens slightly from 5 to 10 ns as the pulse energy increases. Hence, the initial ion velocity distribution remains almost unchanged. Moreover, in the nonthermal regime due to fs laser irradiation, ions are ejected almost instantaneously (i.e., $t_0 \approx 0$ ns). This rapid and spatially limited energy deposition results in a narrow TOF profile. In contrast, for ns laser, the FWHM of the TOF profiles broadens substantially from 13 to 35 ns with increasing pulse energy. This large broadening can be attributed to two interrelated factors. First, the prolonged laser–matter interaction facilitates thermal processes via electron–phonon coupling, which increases T_i and broadens the velocity distribution according to Eq. (1). This thermal velocity spread directly contributes to the broadening of the TOF profile. Second, ion emission duration t_0 increases up to 57 ns at 1000 nJ, which leads to a larger dispersion of the ion arrival times. The increase in t_0 is characteristic of thermally driven ablation, where material removal occurs over a finite period as the target undergoes melting, vaporization, and subsequent hydrodynamic expansion. The combination of these two factors leads to the observed FWHM broadening for ns laser. The increase in t_0 means that ions are continuously emitted from the sample surface even after laser irradiation stops, which is consistent with the results from intensified charge-coupled device observations [11,16].

Both fs and ns lasers exhibit a peak shift corresponding to slower initial ion velocities. However, from Eqs. (5) and (6), both electron energy and ion velocity should increase with increasing laser intensity. This discrepancy suggests that, while Eqs. (5) and (6) provide a reasonable estimate of the energy levels, there are factors not considered in our simulation model regarding the change in the initial ion velocity distribution with laser intensity, such as plasma shielding and spatial inhomogeneity of the laser intensity profile.

Conclusion

We conducted comparative experiments on ion emission for fs and ns laser irradiation using a developed laser ablation TOF mass spectrometer. Combined with ion trajectory simulations, the results demonstrate that fs laser ablation produces ions with higher kinetic energy than ns laser ablation under similar laser pulse energy conditions, whereas ions produced by ns laser irradiation exhibit higher temperatures. For fs laser, the initial energy of the ions calculated from electrostatic ablation is about one-quarter of the value obtained experimentally, suggesting that the ion acceleration mechanism by fs laser irradiation involves another nonthermal process in addition to electrostatic ablation. In addition to the SMBD used to describe the ion initial velocity distribution, we introduce a temporal ion emission process characterized by a Gaussian distribution. Consequently, the TOF profiles of the ions are suitably explained. As the pulse energy increases, ions under ns laser are continuously emitted from the sample surface even after the laser pulse ends. This phenomenon is not observed under fs laser.

CRediT authorship contribution statement

J. Z. Wang: Writing – review & editing, Writing – original draft, Investigation, Formal analysis, Data curation. **Y. Kanematsu:** Supervision. **A. Muratsugu:** Methodology. **F. Matsuda:** Resources. **W. Matsuda:** Resources. **Y. Kawai:** Writing – review & editing, Supervision. **M. Toyoda:** Writing – review & editing, Supervision.

Declaration of competing interest

The authors declare that they have no known competing financial interests or personal relationships that could have appeared to influence the work reported in this paper.

Acknowledgements

The authors gratefully acknowledge Professor Seki of Kyoto University for his valuable contributions to the preparation and surface evaluation of the cesium iodide samples.

Data availability

Data will be made available on request.

References

[1] Sugioka K, Cheng Y. Ultrafast lasers—reliable tools for advanced materials processing. Light Sci Appl 2014;3:e149.
[2] Malinauskas M, Žukauskas A, Hasegawa S, Hayasaki Y, Mizeikis V, Buividas R, et al. Ultrafast laser processing of materials: from science to industry. Light Sci Appl 2016;5:e16133. https://doi.org/10.1038/lsa.2016.133.
[3] Elsied AM, Termini NC, Diwakar PK, Hassanein A. Characteristics of ions emission from ultrashort laser produced plasma. Sci Rep 2016;6:38256. https://doi.org/10.1038/srep38256.
[4] Donnelly T, Krishnamurthy S, Carney K, McEvoy N, Lunney JG. Pulsed laser deposition of nanoparticle films of Au. Appl Surf Sci 2007;254:1303–6. https://doi.org/10.1016/j.apsusc.2007.09.033.
[5] Oba M, Maruyama Y, Akaoka K, Miyabe M, Wakaida I. Double-pulse LIBS of gadolinium oxide ablated by femto- and nano-second laser pulses. Appl Phys A 2010;101:545–9. https://doi.org/10.1007/s00339-010-5894-7.
[6] Fernández B, Claverie F, Pécheyran C, Donard OFX. Direct analysis of solid samples by fs-LA-ICP-MS, TrAC. Trends Anal Chem 2007;26:951–66. https://doi.org/10.1016/j.trac.2007.08.008.
[7] Woryna E, Wolowski J, Králiková B, Krása J, Laska L, Pfeifer M, et al. Laser produced Ag ions for direct implantation. Rev Sci Instrum 2000;71:949–51. https://doi.org/10.1063/1.1150354.
[8] Rethfeld B, Sokolowski-Tinten K, von der Linde D, Anisimov SI. Timescales in the response of materials to femtosecond laser excitation. Appl Phys A 2004;79:767–9. https://doi.org/10.1007/s00339-004-2805-9.
[9] Harilal SS, Freeman JR, Diwakar PK, Hassanein A. Femtosecond laser ablation: Fundamentals and applications. In: Musazzi S, Perini U, editors. Laser-Induced Breakdown Spectroscopy: Theory and Applications. Berlin, Heidelberg: Springer; 2014. p. 143–66.
[10] Leitz KH, Redlingshöfer B, Reg Y, Otto A, Schmidt M. Metal ablation with short and ultrashort laser pulses. Phys Procedia 2011;12:230–8. https://doi.org/10.1016/j.phpro.2011.03.128.
[11] Verhoff B, Harilal SS, Freeman JR, Hassanein A. Dynamics of femto- and nanosecond laser ablation plumes investigated using optical emission spectroscopy. J Appl Phys 2012;112:093302. https://doi.org/10.1063/1.4764060.
[12] Gamaly EG, Rode AV, Luther-Davies B, Tikhonchuk VT. Ablation of solids by femtosecond lasers: Ablation mechanism and ablation thresholds for metals and dielectrics. Phys Plasmas 2002;9:949–57. https://doi.org/10.1063/1.1447555.
[13] Bulgakova NM, Stoian R, Rosenfeld A, Hertel IV, Campbell EEB. Electronic transport and consequences for material removal in ultrafast pulsed laser ablation of materials. Phys Rev B 2004;69:054102. https://doi.org/10.1103/PhysRevB.69.054102.
[14] Gamaly EG, Rode AV, Luther-Davies B, Tikhonchuk VT. Electrostatic mechanism of ablation by femtosecond lasers. Appl Surf Sci 2002;197:699–704. https://doi.org/10.1016/S0169-4332(02)00396-3.
[15] Gamaly EG, Rode AV. Physics of ultra-short laser interaction with matter: from phonon excitation to ultimate transformations. Prog Quantum Electron 2013;37:215–323. https://doi.org/10.1016/j.pquantelec.2013.05.001.
[16] Freeman JR, Harilal SS, Diwakar PK, Verhoff B, Hassanein A. Comparison of optical emission from nanosecond and femtosecond laser produced plasma in atmosphere and vacuum conditions. Spectrochim Acta B At Spectrosc 2013;87:43–50. https://doi.org/10.1016/j.sab.2013.05.011.
[17] Farid N, Harilal SS, Ding H, Hassanein A. Emission features and expansion dynamics of nanosecond laser ablation plumes at different ambient pressures. J Appl Phys 2014;115:033107. https://doi.org/10.1063/1.4862167.
[18] Doggett B, Lunney JG. Expansion dynamics of laser produced plasma. J Appl Phys 2011;109:093304. https://doi.org/10.1063/1.3572260.
[19] Kelly TJ, Butler T, Walsh N, Hayden P, Costello JT. Features in the ion emission of Cu, Al, and C plasmas produced by ultrafast laser ablation. Phys Plasmas 2015;22:123112. https://doi.org/10.1063/1.4937800.
[20] O'Connor A, Morris O, Sokell E. Angular and energy distribution of Sn ion debris ejected from a laser-produced plasma source, for laser power densities in the range suitable for extreme ultraviolet lithography. J Appl Phys 2011;109:073301. https://doi.org/10.1063/1.3558988.
[21] Apinaniz JI, Gordillo-Vázquez FJ, Martínez R. Ion energy distributions in laser-produced plasmas with two collinear pulses. Plasma Sources Sci Technol 2012;21:015016. https://doi.org/10.1088/0963-0252/21/1/015016.
[22] Lin Y, Xu R, Li L, Hang W, He J, Huang B. Kinetic energy and spatial distribution of ions in high irradiance laser ionization source. J Anal At Spectrom 2011;26:1183–90. https://doi.org/10.1039/c1ja00002k.
[23] Shaim MHA, Elsayed-Ali HE. Characterization of laser-generated aluminum plasma using ion time-of-flight and optical emission spectroscopy. J Appl Phys 2017;122:203301. https://doi.org/10.1063/1.4995477.
[24] Harilal SS, Yeak J, Brumfield BE, Suter JD, Phillips MC. Dynamics of molecular emission features from nanosecond, femtosecond laser and filament ablation plasmas. J Anal At Spectrom 2016;31:1192–7. https://doi.org/10.1039/C6JA00036C.
[25] Irimiciuc SA, Nica PE, Agop M, Focsa C. Target properties–plasma dynamics relationship in laser ablation of metals: Common trends for fs, ps and ns irradiation regimes. Appl Surf Sci 2020;506:144926. https://doi.org/10.1016/j.apsusc.2019.144926.
[26] Torrisi L, Gammino S, Andò L, Laska L. Tantalum ions produced by 1064 nm pulsed laser irradiation. J Appl Phys 2002;91:4685–92. https://doi.org/10.1063/1.1446660.
[27] Rai R, Singh BK. Optical and structural properties of CsI thin film photocathode. Nucl Instrum Methods Phys Res, Sect A 785 2015:70–6. https://doi.org/10.1016/j.nima.2015.02.059.
[28] Collado VM, Fernandez-Lima FA, Ponciano CR, Nascimento MAC, Velazquez L, Da Silveira EF. Laser induced formation of CsI ion clusters analyzed by delayed extraction time-of-flight mass spectrometry. PCCP 2005;7:1971–6. https://doi.org/10.1039/B417732K.
[29] Aoki J, Kubo A, Ishihara M, Toyoda M. Simulation of ion trajectories using the surface-charge method on a special purpose computer. Nucl Instrum Methods Phys Res Sect a: Accel Spectrom Detect Assoc Equip 2009;600:466–70. https://doi.org/10.1016/j.nima.2008.11.095.
[30] Zhilinsky AP. Fundamentals of Plasma Physics. John Wiley & Sons; 1980.
[31] Apinaniz JI, Sierra B, Martinez R, Longarte A, Redondo C, Castaño F. Ion kinetic energy distributions and mechanisms of pulsed laser ablation on Al. J Phys Chem C 2008;112:16556–60. https://doi.org/10.1021/jp805610h.
[32] Mannion PT, Favre S, Mullan C, Ivanov DS, O'Connor GM, Glynn TJ, et al. Langmuir probe investigation of plasma expansion in femto- and picosecond laser ablation of selected metals. J Phys Conf Ser 2007;59:753. https://doi.org/10.1088/1742-6596/59/1/161.
[33] Rozmus W, Tikhonchuk VT. Skin effect and interaction of short laser pulses with dense plasmas. Phys Rev A 1990;42:7401. https://doi.org/10.1103/PhysRevA.42.7401.
[34] Benson JM, Novak I, Potts AW. Photoelectron spectroscopy of the caesium halides using synchrotron radiation. J Phys B: At Mol Phys 1987;20:6257. https://doi.org/10.1088/0022-3700/20/23/017.
[35] Su TMR, Riley SJ. Alkali halide photofragment spectra. I. Alkali iodide bond energies and excited state symmetries at 266 nm. J Chem Phys 1979;71:3194–202. https://doi.org/10.1063/1.438766.
[36] Stoian R, Ashkenasi D, Rosenfeld A, Campbell EEB. Coulomb explosion in ultrashort pulsed laser ablation of Al_2O_3. Phys Rev B 2000;62:13167. https://doi.org/10.1103/PhysRevB.62.13167.
[37] Zhigilei LV, Leveugle E, Garrison BJ, Yingling YG, Zeifman MI. Computer simulations of laser ablation of molecular substrates. Chem Rev 2003;103:321–48. https://doi.org/10.1021/cr010459r.
[38] M. V. Shugaev, M. He, Y. Levy, A. Mazzi, A. Miotello, N. M. Bulgakova, L. V. Zhigilei, Laser-induced thermal processes: heat transfer, generation of stresses, melting and solidification, vaporization, and phase explosion, in: Handbook of Laser Micro- and Nano-Engineering, Springer, Cham (2021) 83–163. doi:10.1007/978-3-030-63647-0_11.
[39] Hada M, Zhang D, Pichugin K, Hirscht J, Kochman MA, Hayes SA, et al. Cold ablation driven by localized forces in alkali halides. Nat Commun 2014;5:3863. https://doi.org/10.1038/ncomms4863.
[40] Wu C, Zhigilei LV. Microscopic mechanisms of laser spallation and ablation of metal targets from large-scale molecular dynamics simulations. Appl Phys A 2014;114:11–32. https://doi.org/10.1007/s00339-013-8086-4.